NANOMATERIALS

Ligand-protected metal nanoclusters as low-loss, highly polarized emitters for optical waveguides

Xiaojian Wang[1]†, Bing Yin[1]†, Lirong Jiang[1]†, Cui Yang[2], Ying Liu[1], Gang Zou[2], Shuang Chen[1]*, Manzhou Zhu[1]*

Photoluminescent molecules and nanomaterials have potential applications as active waveguides, but such a use has often been limited by high optical losses and complex fabrication processes. We explored ligand-protected metal nanoclusters (LPMNCs), which can have strong, stable, and tunable emission, as waveguides. Two alloy LPMNCs, Pt_1Ag_{18} and Au_xAg_{19-x} ($7 \leq x \leq 9$), were synthesized and structurally determined. Crystals of both exhibited excellent optical waveguide performance, with optical loss coefficients of 5.26×10^{-3} and 7.77×10^{-3} decibels per micrometer, respectively, lower than those demonstrated by most inorganic, organic, and hybrid materials. The crystal packing and molecular orientation of the Pt_1Ag_{18} compound led to an extremely high polarization ratio of 0.91. Aggregation enhanced the quantum yields of Pt_1Ag_{18} and Au_xAg_{19-x} LPMNCs by 115- and 1.5-fold, respectively. This photonic cluster with low loss and high polarization provides a generalizable and versatile platform for active waveguides and polarizable materials.

Optical waveguide systems can be made of passive elements based on refractive index changes, as in an optical fiber, or of active elements that create gain or introduce nonlinear optical effects for signal amplification (1–3). For molecular active optical waveguides, dipole orientations affect the direction of photon transmission. (4–9) Reported active waveguide materials, such as organic chromophores, hybrid materials, and polymer materials, have had drawbacks such as high loss, complex synthesis, and low yield (6, 8–15). Ligand-protected metal nanoclusters (LPMNCs), which are composed of a few to hundreds of metal atoms and surface ligands (16–21), are suitable for optical waveguide materials (16, 22). They have strong, stable and tunable emission, good photostability, a large Stokes shift, and high quantum yields (QYs) (23, 24) and can be synthesized in high purity and yield. For waveguide applications, aggregation-induced emission enhancement could further enhance the photoluminescence (PL) of LPMNCs (25, 26).

We report the optical waveguide performance of two LPMNCs, $[Pt_1Ag_{18}(S\text{-}Adm)_2(DPPP)_6Cl_6](SbF_6)(AgCl_2)$ (hereafter referred to as Pt_1Ag_{18}, where S-Adm is adamantane mercaptan and DPPP is 1,3-bis-diphenylphosphine propane)

[1]Institute of Physical Science and Information Technology, Key Laboratory of Structure and Functional Regulation of Hybrid Materials of Ministry of Education, Center for Atomic Engineering of Advanced Materials, Anhui Province Key Laboratory of Chemistry for Inorganic/Organic Hybrid Functionalized Materials, Anhui University, Hefei, Anhui 230601, P. R. China. [2]CAS Key Laboratory of Soft Matter Chemistry, Collaborative Innovation Center of Chemistry for Energy Materials (iChEM), Department of Polymer Science and Engineering, University of Science and Technology of China, Hefei, Anhui 230601, P. R. China.
*Corresponding author. Email: chenshuang@ahu.edu.cn (S.C.); zmz@ahu.edu.cn (M.Z.)
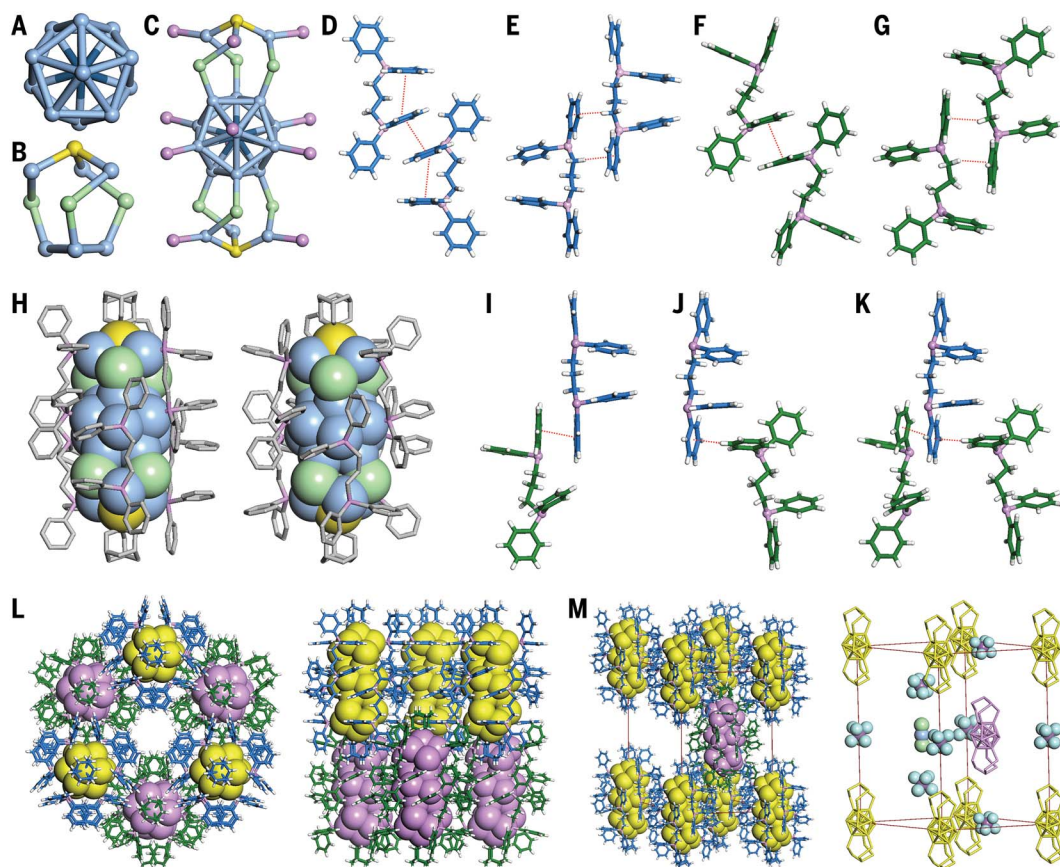†These authors contributed equally to this work.

and $[Au_xAg_{19-x}(S\text{-}Adm)_2(DPPP)_6Cl_6](ClO_4)_3$ (hereafter referred to as Au_xAg_{19-x}, where $7 \leq x \leq 9$), both of which had rod-like structures and strong emission properties. The emission spectra of Pt_1Ag_{18} and Au_xAg_{19-x} were orange and red and were centered at 600 and 770 nm, respectively. One-dimensional (1D) microrod crystals of these LPMNCs exhibited excellent optical waveguide performance, with low optical loss coefficients and distinct polarized waveguide performance. The polarization ratios of Pt_1Ag_{18} and Au_xAg_{19-x} were 0.91 and 0.17, respectively, which we attributed to the differences in their crystal structure and packing modes. Both LPMNCs displayed aggregation-induced emission enhancement in that the QYs of Pt_1Ag_{18} and Au_xAg_{19-x} in the solid state were 115 and 1.5 times higher than those in solution, respectively. We propose that Pt_1Ag_{18} and Au_xAg_{19-x}, along with other LPMNCs, could find applications in optoelectronic devices.

Crystal structure of Pt_1Ag_{18}

We prepared Pt_1Ag_{18} ligand-protected nanoclusters (NCs) by reacting Pt_1Ag_{28} NCs (27) with $Ag_2(DPPP)Cl_2$ complexes in dichloromethane (see the supplementary materials), and their structure was determined to be $[Pt_1Ag_{18}(S\text{-}Adm)_2(DPPP)_6Cl_6](SbF_6)(AgCl_2)$ by single-crystal x-ray diffraction (SCXRD) (table S1 and Fig. 1). The Pt_1Ag_{18} structure consisted of a kernel composed of a central Pt atom and 12 Ag atoms (Fig. 1A) surrounded by a shell composed of six DPPP ligands (Fig. 1C) and two crown-like $Ag_3Cl_3(S\text{-}Adm)_1$ staple motifs (Fig. 1B). The two $Ag_3Cl_3(S\text{-}Adm)_1$ motifs of the surface shell were distributed on each side of the Pt_1Ag_{12} kernel, and each motif was connected to the Ag atoms in the kernel through three Ag–Cl bonds with a bond length of 2.44 Å, forming a rod-like $Pt_1Ag_{18}Cl_6(DPPP)_6(S\text{-}Adm)_2$

structure. The two P atoms in each of the six DPPP ligands bonded to the Ag atoms in both the crown-like motif and the Pt_1Ag_{12} kernel in a form parallel to the $Pt_1Ag_{18}Cl_6(S\text{-}Adm)_2$ rod (Fig. 1C), leading to the total structure of $[Pt_1Ag_{18}(S\text{-}Adm)_2(DPPP)_6Cl_6]^{2+}$ (Fig. 1H).

Each crystal cell contained two Pt_1Ag_{18} molecules with the counterions SbF_6^- and $AgCl_2^-$ (Fig. 1M); one was at the apex of the unit cell (Pt_1Ag_{18}-1, yellow highlights in Fig. 1M), and the other was in the center (Pt_1Ag_{18}-2, pink highlights in Fig. 1M). An important difference between the two Pt_1Ag_{18} clusters in each unit cell was the pattern of their associated DPPP benzene rings (Fig. 1H), which resulted in differing intermolecular and intramolecular noncovalent interactions. In Pt_1Ag_{18}-1, $\pi...\pi$ interactions within each DPPP ligand and between adjacent DPPP ligands were observed (Fig. 1D), whereas in Pt_1Ag_{18}-2, $\pi...\pi$ interactions were only observed between two adjacent DPPP ligands (Fig. 1F). The bonding patterns of the three DPPP methylene groups in Pt_1Ag_{18}-1 (Fig. 1E) and Pt_1Ag_{18}-2 were also different and led to differences in noncovalent interactions. The C–H bonds of the DPPP methylene groups interacted with the benzene π electrons, forming C–H...π secondary bonds for Pt_1Ag_{18}-1 and Pt_1Ag_{18}-2 (Fig. 1, E and G, respectively).

In layered Pt_1Ag_{18}-1 and Pt_1Ag_{18}-2, $\pi...\pi$ intermolecular interactions were evident between the top and bottom benzene rings of the DPPP ligands (Fig. 1I), and the C–H bonds of the benzene rings in Pt_1Ag_{18}-2 interacted with π electrons in Pt_1Ag_{18}-1 (Fig. 1J), which together induced C–H...$\pi...\pi$ intermolecular interactions (Fig. 1K). Such interactions increased the rigidity and stability of Pt_1Ag_{18}, facilitating its crystallization, and were similar to the interactions associated with the self-assembly of organic molecules. From the [001] crystallographic direction, Pt_1Ag_{18}-1 and Pt_1Ag_{18}-2 alternated to form an orthohexagonal pattern (Fig. 1L, left). From the [100] crystallographic direction, layered stacking of the Pt_1Ag_{18}-1 and Pt_1Ag_{18}-2 orthohexagonal structures can be observed (Fig. 1L). Thus, the differing intermolecular and intramolecular noncovalent interactions of the benzene rings affected the crystallization and self-assembly of the LPMNCs.

Crystal structure of Au_xAg_{19-x}

Au_xAg_{19-x} NCs were prepared in a one-pot synthesis. A mixture of DPPP and HS-Adm was added to a solution of $AgNO_3$ in ethanol, and then an aqueous solution of $HAuCl_4$ was introduced, followed by an aqueous solution of $NaBH_4$ (see the supplementary materials), and their structure was determined to be $[Au_xAg_{19-x}(S\text{-}Adm)_2(DPPP)_6Cl_6](ClO_4)_3$ by single-crystal x-ray crystallography (table S2 and Fig. 2). The Au_xAg_{19-x} structure consisted

Fig. 1. Crystal structure of Pt₁Ag₁₈. (A to C) Pt₁Ag₁₂ kernel (A), Ag₃Cl₃S motif (B), and structure (C) of the Pt₁Ag₁₈Cl₆(DPPP)₆(S-Adm)₂ rod. (D) Intramolecular π...π interaction in **Pt₁Ag₁₈-1**. (E) Intramolecular C−H...π interaction in **Pt₁Ag₁₈-1**. (F) Intramolecular π...π interaction in **Pt₁Ag₁₈-2**. (G) Intramolecular C−H...π interaction in **Pt₁Ag₁₈-2**. (H) Overall structure of **Pt₁Ag₁₈-1** [left, yellow highlights in (L) and (M)] and **Pt₁Ag₁₈-2** [right, pink highlights in (L) and (M)]. (I) Intermolecular π...π interaction between **Pt₁Ag₁₈-1** and **Pt₁Ag₁₈-2**. (J) Intermolecular C−H...π interaction between **Pt₁Ag₁₈-1** and **Pt₁Ag₁₈-2**. (K) Interaction between **Pt₁Ag₁₈-1** and **Pt₁Ag₁₈-2**. (L) Orthohexagonal packing pattern for **Pt₁Ag₁₈-1** and **Pt₁Ag₁₈-2**. (M) A unit cell of Pt₁Ag₁₈. C and H atoms have been omitted for clarity in (A) to (C). H atoms have been omitted for clarity in (H). C, H, and P atoms have been omitted for clarity in the right side of (M). The intramolecular and intermolecular interactions are indicated by red dotted lines in (D) to (G) and (I) to (K).

of an Au₇Ag₆ kernel and an (AuAg)₆Cl₆(S-Adm)₂(DPPP)₆ shell (Fig. 2C). In the Au₇Ag₆ kernel, Ag₃, Au₇, and Ag₃ were stacked sequentially in layers (Fig. 2A). The shell was composed of two crown-like M₃Cl₃(S-Adm)₁ staple motifs (Fig. 2B, where M is a metal, i.e., Au or Ag) and six DPPP ligands (Fig. 2C). The three metal sites in each of the two M₃Cl₃(S-Adm)₁ staple motifs were occupied by either Au or Ag. The two M₃Cl₃(S-Adm)₁ motifs were connected to the Ag atoms on the Au₇Ag₆ kernel through three M–Cl bonds with a bond length of 2.36 Å. Six DPPP ligands bonded to the metal atoms in the staple motifs and the exterior Au atoms of the Au₇Ag₆ kernel through their P atoms. The P–Au–S bond angle was larger than the P–Ag–S bond angle; the average angles were 173.56° and 144.20°, respectively. The resulting total structure of [AuₓAg₁₉₋ₓ(S-Adm)₂(DPPP)₆Cl₆]³⁺ is shown in Fig. 2D.

Each crystal cell contained two AuₓAg₁₉₋ₓ molecules with six ClO₄⁻ counterions (Fig. 2N).

Unlike Pt₁Ag₁₈, the patterns of the associated benzene rings of the two AuₓAg₁₉₋ₓ molecules in each unit cell were the same (Fig. 2D). However, the orientations of the two AuₓAg₁₉₋ₓ NCs were different. In a single molecule of AuₓAg₁₉₋ₓ, π...π interactions in a single DPPP ligand and between two DPPP ligands were observed (Fig. 2, E to G). The C–H bonds from the DPPP methylene groups also interacted with the benzene π electrons, forming a C–H...π interaction between two ligands (Fig. 2, H to J). The C–H bonds of the benzene rings in each AuₓAg₁₉₋ₓ NCs formed either C–H...π, C–H...π...H–C, or C–H...π...π interactions with the π electrons in the other adjacent AuₓAg₁₉₋ₓ NCs (Fig. 2, K and L). Such interactions facilitated crystallization. The different metal atoms and different intermolecular and intramolecular interactions of Pt₁Ag₁₈ and AuₓAg₁₉₋ₓ led to different packing patterns. AuₓAg₁₉₋ₓ formed a zigzag pattern along the [100] crystallographic direction (Fig. 2M).

Characterization of Pt₁Ag₁₈ and AuₓAg₁₉₋ₓ

The Pt₁Ag₁₈ and AuₓAg₁₉₋ₓ NCs were further characterized by ultraviolet-visible (UV-vis) spectroscopy, electrospray ionization mass spectrometry (ESI-MS), x-ray photoelectron spectroscopy, and thermogravimetric analysis. The UV-vis absorption spectrum of Pt₁Ag₁₈ (fig. S1) includes peaks centered at ~330, 365, and 490 nm (fig. S1A); the energy difference between highest-occupied and lowest-unoccupied molecular orbitals (i.e., the HOMO-LUMO gap) was estimated to be 1.92 eV (fig. S1B). The UV-vis absorption spectrum of AuₓAg₁₉₋ₓ had peaks centered at ~353, 427, 483, and 545 nm (fig. S2A), corresponding to a HOMO-LUMO gap of 1.97 eV (fig. S2B). The multiple absorption peaks revealed the quantum size effect of Pt₁Ag₁₈ and AuₓAg₁₉₋ₓ NCs, which is different from the surface plasmon resonance of nanoparticles.

The ESI-MS spectrum of Pt₁Ag₁₈ had a mass-to-charge (m/z) peak centered at 2579.69 (fig. S3), which corresponded to [Pt₁Ag₁₈(DPPP)₆
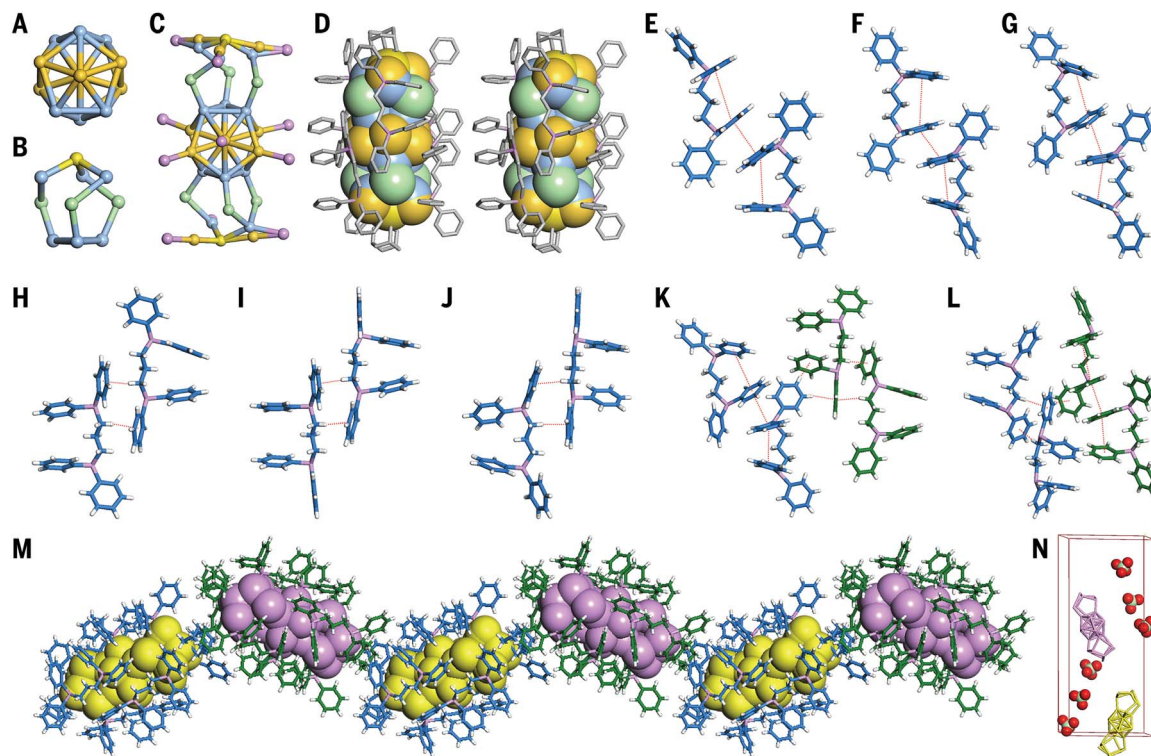
Fig. 2. Crystal structure of Au$_x$Ag$_{19-x}$. (**A** to **C**) Au$_7$Ag$_6$ kernel (A), M$_3$Cl$_3$(S-Adm)$_1$ motifs (B), and structure (C) of Au$_x$Ag$_{19-x}$Cl$_6$(DPPP)$_6$(S-Adm)$_2$. (**D**) Overall structure of Au$_x$Ag$_{19-x}$. (**E** to **G**) Intramolecular π...π interaction in Au$_x$Ag$_{19-x}$. (**H** to **J**) Intramolecular C–H...π interaction between two DPPP ligands. (**K** and **L**) Intermolecular C–H...π, C–H...π...H–C, and C–H...π...π interaction in Au$_x$Ag$_{19-x}$. (**M**) 1D packing pattern for Au$_x$Ag$_{19-x}$. (**N**) A unit cell of Au$_x$Ag$_{19-x}$. C and H atoms have been omitted for clarity in (A) to (C). H atoms have been omitted for clarity in (D). C, H, and P atoms have been omitted for clarity in (N). The intramolecular and intermolecular interactions are indicated by red dotted lines in (E) to (L).

(S-Adm)$_2$Cl$_6$]$^{2+}$ (calculated formula weight: 2579.58). The ESI-MS spectrum of Au$_x$Ag$_{19-x}$ showed a series of six peaks corresponding to [Au$_x$Ag$_{19-x}$(S-Adm)$_2$(DPPP)$_6$Cl$_6$(ClO$_4$)$_1$]$^{2+}$ and [Au$_x$Ag$_{19-x}$(S-Adm)$_2$(DPPP)$_6$Cl$_6$]$^{3+}$, with 7 ≤ x ≤ 9 (fig. S4). These data were consistent with the results obtained by SCXRD. x-ray photoelectron spectroscopy of Pt$_1$Ag$_{18}$ (figs. S5 and S6) and Au$_x$Ag$_{19-x}$ (figs. S7 and S8) confirmed the presence of all of the expected elements. Thermogravimetric analysis of Pt$_1$Ag$_{18}$ showed a total weight loss of 54.7 wt % (fig. S9A), which is consistent with the theoretical loss (53.96 wt %) calculated based on the formula determined from x-ray crystallography. Similarly, the total weight loss of 49.64% is consistent with the theoretical value for [Au$_{10.1}$Ag$_{8.9}$(S-Adm)$_2$(DPPP)$_6$Cl$_6$](ClO$_4$)$_3$ (fig. S9B).

Pt$_1$Ag$_{18}$ and Au$_x$Ag$_{19-x}$ microrods as optical waveguides

We investigated the photonic properties of Pt$_1$Ag$_{18}$ and Au$_x$Ag$_{19-x}$ NCs by optical waveguide. Both Pt$_1$Ag$_{18}$ and Au$_x$Ag$_{19-x}$ NCs readily formed defect-free single crystals with smooth surfaces (fig. S10) through multiple noncovalent interactions within their structures and their high synthesis purities, thereby ensuring high PL efficiency and minimal light scatter-

ing from the domain boundary. Fluorescence microscopy was applied to hexagonal sheets of Pt$_1$Ag$_{18}$ and Au$_x$Ag$_{19-x}$ to monitor their PL. Under unfocused irradiation, the edges of the Pt$_1$Ag$_{18}$ and Au$_x$Ag$_{19-x}$ crystals were brighter than the center, indicating their optical waveguide behavior (Fig. 3, B and C).

Next, spatially resolved PL imaging was performed on 1D microrod crystals of Pt$_1$Ag$_{18}$ and Au$_x$Ag$_{19-x}$ to evaluate the optical waveguide efficiency (Fig. 3A) by moving a focused excitation laser beam (450 nm) to different local positions along the microrod crystal body. Photons propagated predominantly along both directions of the axis of the 1D microrod crystals in two predominant transmission directions (Fig. 3, D and E). The emission intensity at the tip of the microrod decreased with increasing propagation distance, but the spectral intensity and profiles of the excited points were constant.

To quantify the optical loss of the microrod crystals, we calculated the optical loss coefficient (R) by single-exponential fitting: $I_{tip}/I_{body} = A \exp(-RD)$, where I_{tip} and I_{body} are the intensities at the emitted tip and the excited site, respectively, and D is the distance between the excited site and the emitted tip (Fig. 3, D and E). In the Pt$_1$Ag$_{18}$ microrod, R was calculated to be 5.26 × 10^{-3} dB μm^{-1}, and

in the Au$_x$Ag$_{19-x}$ microrod, it was calculated to be 7.77 × 10^{-3} dB μm^{-1}. These values exhibited high consistency across different microrods from the same and different batches (figs. S11 to S13), indicating good repeatability. These values are lower than those previously reported for inorganic (*12*), organic (*1, 6, 8, 10, 11, 15*), and hybrid materials (*9, 28*), the R values of which range from ~10 to 60 × 10^{-3} dB μm^{-1}, and are indicative of high optical waveguide efficiency. Intramolecular interactions of the NCs inhibited nonradiative transitions. Intermolecular interactions, which result in denser crystal packing, high levels of crystallinity, and smooth surfaces, helped to diminish emission losses by scattering.

The optical waveguides of the microrods exhibited stability, with the Au$_x$Ag$_{19-x}$ microrod displaying higher stability than the Pt$_1$Ag$_{18}$ microrod at a temperature of 50°C in an air environment (figs. S14 to S16). The observed increase in optical loss over time could be attributed to the evaporation of solvent molecules within the crystals under high-temperature and oxygen-rich conditions. Furthermore, the microrods composed of NCs demonstrated excellent stability when subjected to various solvents. As shown in figs. S17 to S19, the Au$_x$Ag$_{19-x}$ microrod displayed a reduced loss coefficient when treated with toluene, p-xylene,

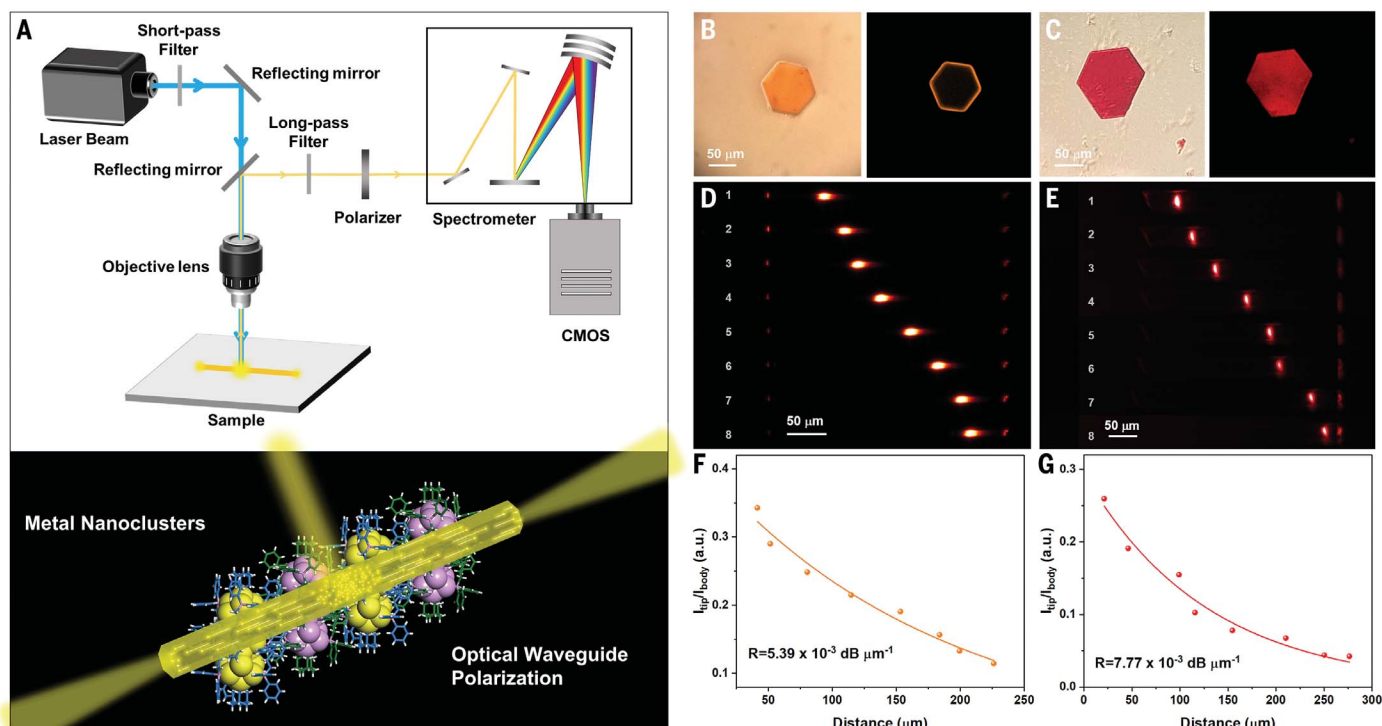**Fig. 3. Optical waveguide of Pt$_1$Ag$_{18}$ and Au$_x$Ag$_{19-x}$.** (**A**) Experimental setup for the optical waveguide equipment. (**B** and **C**) Photographs of hexagonal sheets of Pt$_1$Ag$_{18}$ and Au$_x$Ag$_{19-x}$ under visible light (left) and fluorescence microscopy images under unfocused 405 nm irradiation (right). (**D** and **E**) PL images of microrod crystals of Pt$_1$Ag$_{18}$ and Au$_x$Ag$_{19-x}$ excited with a 450 nm laser focused at different positions.

Numbers 1 to 8 correspond to PL images of excitation along the microrod crystal body from left to right. (**F** and **G**) Ratio of the intensities at the tip and body of microrod crystals (I_{tip}/I_{body}) of Pt$_1$Ag$_{18}$ and Au$_x$Ag$_{19-x}$ versus the distance between the excitation and emission spots on the right side of the images in (D) and (E). The curve was fitted by the exponential decay function $I_{tip}/I_{body} = A \exp(-RD)$.

and c-pentane, whereas the Pt$_1$Ag$_{18}$ microrod exhibited a slight increase in the loss coefficient when treated with p-xylene, c-pentane, and t-butyl methyl ether. Solvents may affect the weak interactions within the microrods, thereby influencing the optical waveguide performance of NCs.

We observed that NC crystals in bent and branched states exhibited significant optical waveguide effects (figs. S20 and S21). The formation of bent crystals can be attributed to the flexibility of surface organic ligands and the intermolecular interactions of NCs. The waveguides formed by NCs in bent and branched states provide opportunities for photonic propagation within miniaturized complex structures. Additionally, both NC 2D crystal microsheets exhibited optical waveguiding, and we further investigated their waveguide directionality. As shown in figs. S22 and S23, the luminescence intensities of each side of the microsheets were virtually identical when excited in the center. When one side of the crystal was excited, the other sides exhibited similar emission intensities. These results indicate the absence of anisotropy in the optical waveguide behavior. However, optical waveguide behavior was barely observed in the amorphous powder state (fig. S24) and film state (fig. S25) of the

NCs, which can be attributed to the limited ability of photons to propagate in the absence of highly ordered structures of NCs.

We studied whether other LPMNCs could exhibit the optical waveguide properties, and found that Au$_4$Cu$_5$ (*29*), Au$_1$Cu$_{14}$ (*30*), and Pt$_1$Ag$_{37}$ (*31*) also exhibited low R, with $R = 13.21 \times 10^{-3}$ dB μm^{-1} for Au$_4$Cu$_5$, 15.88×10^{-3} dB μm^{-1} for Au$_1$Cu$_{14}$, and 9.92×10^{-3} dB μm^{-1} for Pt$_1$Ag$_{37}$ (fig. S26). We further studied the effect of Stokes shifts of all of these LPMNCs on R. The large Stokes shifts of NCs correspond to a narrow overlap in the emission and main absorption spectra and effectively diminished reabsorption of light during propagation along the crystals. However, R did not decrease with the increase of Stokes shifts (fig. S27), which indicated that the Stokes shift was not the only factor affecting the optical loss coefficient of metal NCs. Smooth surfaces and high crystal quality also have important effects on optical waveguide properties (*22*, *32*).

Polarized optical performance of Pt$_1$Ag$_{18}$ and Au$_x$Ag$_{19-x}$

The optical properties of emitters are directly affected by the packing of their constituent molecules and the orientation of their optical transition dipoles. In particular, packing and

orientation lead to distinct PL polarization, an effect that is important for waveguide design, optical connections, and active optical communication device integration. To elucidate the optical anisotropy caused by the orientation of the molecules in the microrods, polarized optical microscopy was performed. By rotating the polarizer to different polarization angles (θ), the linear polarization of the light signal emitted from the tips of microrods of Pt$_1$Ag$_{18}$ and Au$_x$Ag$_{19-x}$ could be obtained. We measured θ as the angle between the horizontal direction of the 1D crystal and the polarization direction of the polarizer placed in front of the charge-coupled device detector (Fig. 3A) and recorded the PL intensities of the polarized light signals from the tip at 30° increments (Fig. 4).

The relationship between the maximum luminous intensity and the polarization angle of the microrod crystals was well with a sin^2 curve. The Pt$_1$Ag$_{18}$ microrod displayed the highest fluorescence intensities at polarized angles of 8° and 188° and the lowest at 98° and 278° (Fig. 4A), leading to an emission dichroic ratio ($R_d = I_{8°}/I_{98°}$) of 21.4 and a polarization ratio [$ρ = (R_d - 1)/(R_d + 1)$] of 0.91, which was beneficial to materials. However, Au$_x$Ag$_{19-x}$ microrods exhibited weak polarization properties,

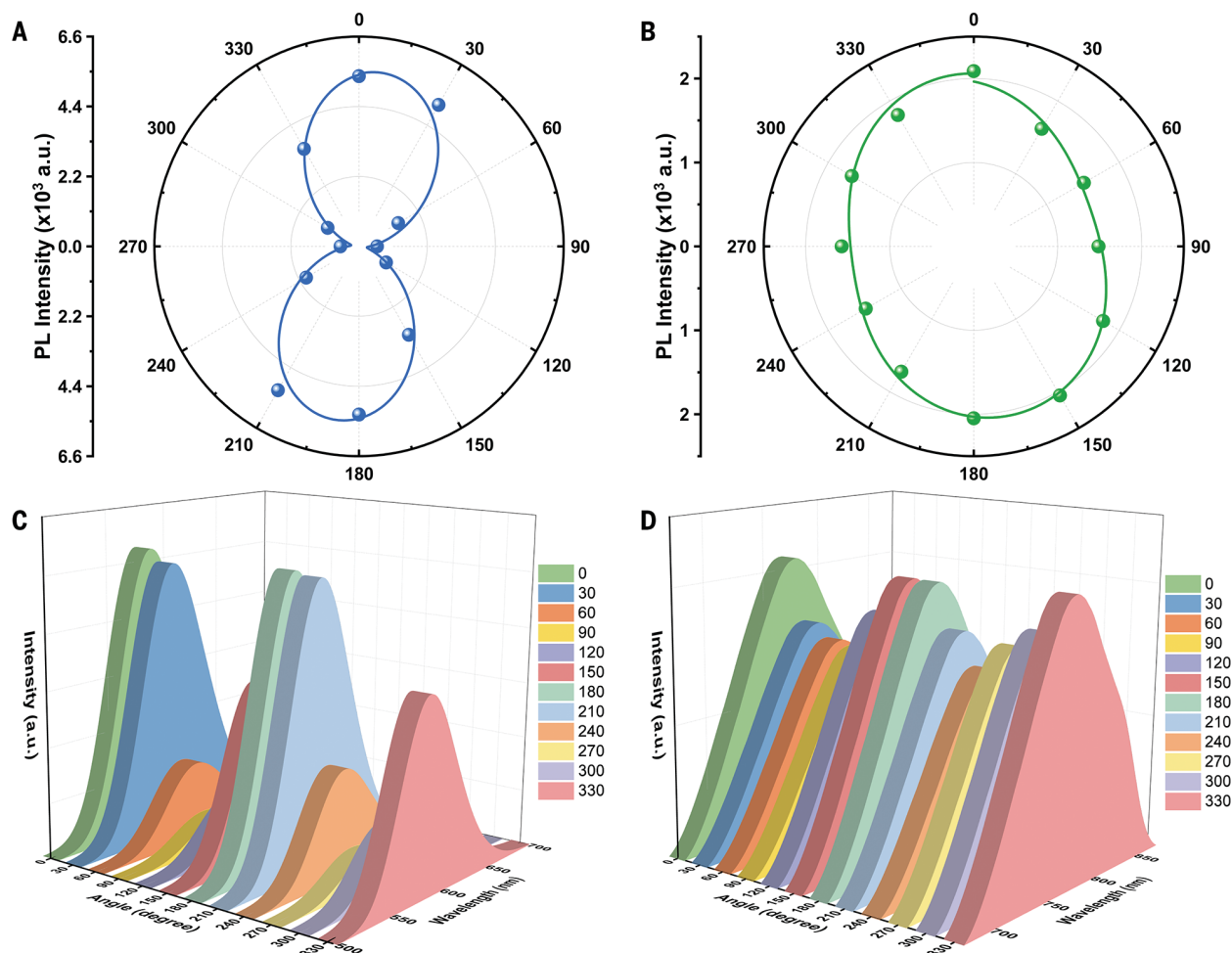**Fig. 4. Polarized optical performance of Pt₁Ag₁₈ and AuₓAg₁₉₋ₓ.** (**A** and **B**) Photoemission intensity of the Pt_1Ag_{18} and Au_xAg_{19-x}, respectively, as a function of the polarizer rotation angle θ. (**C** and **D**) Polarized PL spectra of Pt_1Ag_{18} and Au_xAg_{19-x} microrods, respectively, at various angles (~0 to 360°).

with a ρ of 0.17, as calculated from its highest and lowest PL intensities at 174° and 71°, respectively.

Observation of the molecular orientations of Pt_1Ag_{18} and Au_xAg_{19-x} (Figs. 1M and 2M), the angle between the transition dipole moment of the Pt_1Ag_{18} NCs, and their preferred direction of growth results in high polarization emission. For Au_xAg_{19-x} microrods, however, the weak PL anisotropy detected was attributed to the zigzag pattern in which the two molecules in each unit cell pack together (Fig. 2M). Thus, the differences in the polarization properties of Pt_1Ag_{18} and Au_xAg_{19-x} can be attributed to the partially anisotropic structure of NC entities and their incomplete mirror symmetry packing modes (*33*).

PL properties

We further explored the emissions of Pt_1Ag_{18} and Au_xAg_{19-x} as amorphous solids and in dichloromethane solution by measuring their QY, defined as the ratio of emitted photons to absorbed photons, and their PL lifetime. The solution of Pt_1Ag_{18} was weakly emissive; the

maximum emission was centered at 600 nm under an excitation of 366 nm (Fig. 5A) with a QY of 0.25%. By comparison, solid Pt_1Ag_{18} exhibited an intense orange emission (Fig. 5B) with a much higher QY of 28.9%. The average PL lifetime of Pt_1Ag_{18} was also improved in the solid state, with the lifetimes in solution and in the solid state of 0.54 and 1.88 μs, respectively (fig. S28). This trend held, although with smaller increases, for Au_xAg_{19-x}. In solution, Au_xAg_{19-x} displayed a weak red emission at 770 nm with a QY of 4.66% under excitation at 467 nm (Fig. 5, A and B), but a slightly stronger emission was observed in the solid state, with a QY of 6.91%. The average PL lifetimes of Au_xAg_{19-x} similarly had a small increase in the solid state, as the lifetime in solution and in the solid state were 2.68 and 3.17 μs, respectively (fig. S29). The differences in emission between Pt_1Ag_{18} and Au_xAg_{19-x} can be attributed to the alloy effect, which influences the origin of the PL.

This difference in the emissions of Pt_1Ag_{18} and Au_xAg_{19-x} in different states led us to further explore their aggregation-induced emis-

sion enhancement (AIEE) performance. We analyzed solutions of each material in mixtures of acetonitrile (MeCN) and H_2O, selected for their ability to dissolve the two NCs readily and poorly, respectively. The PL intensity of Pt_1Ag_{18} was enhanced 30-fold as the proportion of water in the binary solvent mixture increased, reaching a maximum value of PL at a 4:6 volume ratio of MeCN:H_2O (Fig. 5C). Increasing the proportion of water >60% decreased the emissions, but the PL was still much higher than that in pure MeCN. Similar results were observed previously in other AIEE active materials (*34*).

Dynamic light scattering was used to evaluate the aggregation degree and size distribution of Pt_1Ag_{18}, showing that the aggregation of the NCs was highest at 4:6 MeCN:H_2O, with an average aggregate diameter of 342 nm (range 220 to 531 nm) (fig. S30), thus confirming the relationship between increased aggregation and increased PL emission. Similar results were observed in solutions of Au_xAg_{19-x}, with a fivefold enhancement in the PL intensity of strong red emissions at a MeCN:H_2O volume
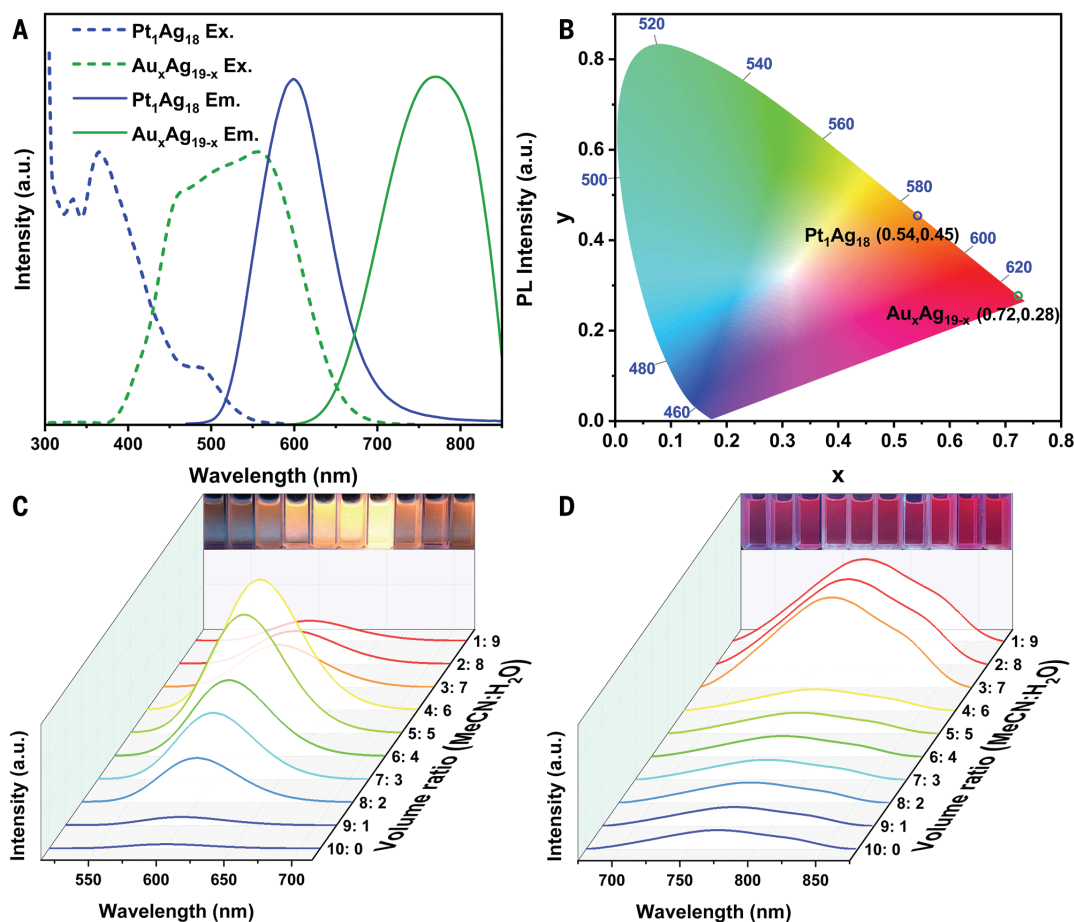
Fig. 5. PL of Pt₁Ag₁₈ and AuₓAg₁₉₋ₓ. (**A**) Excitation (blue dashed line) and emission (blue solid line) spectra of Pt₁Ag₁₈ in solution and the excitation (green dashed line) and emission (green solid line) spectra of AuₓAg₁₉₋ₓ in solution. (**B**) Commission Internationale de l'Eclairage (CIE) chromaticity coordinates of the PL of Pt₁Ag₁₈ (blue circle) and AuₓAg₁₉₋ₓ (green circle). (**C** and **D**) Photoemission spectra of Pt₁Ag₁₈ and AuₓAg₁₉₋ₓ, respectively, in mixed solvents of MeCN and H₂O with different volume ratios. Insets: digital photos of Pt₁Ag₁₈ and AuₓAg₁₉₋ₓ in mixed solvents with different volume ratios under 365 nm UV light irradiation.

ratio of 3:7 (Fig. 5D) caused by the maximum degree of aggregation (fig. S31).

To evaluate the effect of aggregation on absorption, UV-vis absorption spectra of Pt₁Ag₁₈ and AuₓAg₁₉₋ₓ in various mixed solvent systems were collected. As shown in fig. S32A, neither a shift in absorption peak nor a change in relative intensity was observed across 10 different solvent mixtures, suggesting that the aggregation of Pt₁Ag₁₈ is not associated with decomposition or structural changes. As shown in fig. S32B, the UV-vis absorption spectra of AuₓAg₁₉₋ₓ in 10 mixed solvent systems also showed no absorption peak shift or relative intensity change. Both Pt₁Ag₁₈ and AuₓAg₁₉₋ₓ NCs exhibited AIEE performance without decomposition or structural changes to the ligand-protected NCs, although the PL enhancement of Pt₁Ag₁₈ was more pronounced.

Conclusions

Here, we synthesized and characterized ligand-protected Pt₁Ag₁₈ and AuₓAg₁₉₋ₓ NCs and studied their optical waveguide properties.

Both NCs consist of an icosahedral M₁₃ core, two crown-like M₃Cl₃(SR)₁ staple motifs, and six DPPP ligands. Crystals of the Pt₁Ag₁₈ and AuₓAg₁₉₋ₓ NCs exhibited excellent optical waveguide performance, with low optical loss coefficients of 5.26×10^{-3} and 7.77×10^{-3} dB μm⁻¹, respectively, which can be attributed to their inhibition of nonradiative transition, dense crystal packing, and large Stokes shifts. Furthermore, the optical waveguide performance of other NCs was investigated, which revealed the universality among ligand-protected, atomically precise NCs. The different crystal structures and packing modes of Pt₁Ag₁₈ and AuₓAg₁₉₋ₓ account for their distinct polarized waveguide performance. Pt₁Ag₁₈ microrods displayed excellent polarizing properties with a polarization ratio of 0.91, whereas AuₓAg₁₉₋ₓ microrods showed weak polarized emission with a polarization ratio of 0.17. Furthermore, Pt₁Ag₁₈ and AuₓAg₁₉₋ₓ displayed an AIEE effect, and 115- and 1.5-fold enhancements in QY were observed for Pt₁Ag₁₈ (28.9% versus 0.25%) and AuₓAg₁₉₋ₓ (6.91% versus 4.66%) from the

solid state to solution. Collectively, these results suggest that Pt₁Ag₁₈ and AuₓAg₁₉₋ₓ NCs have potential for use in optical communication and miniaturized optoelectronic devices.

REFERENCES AND NOTES

1. S. Wu, B. Zhou, D. Yan, *Adv. Opt. Mater.* **9**, 2001768 (2021).
2. Y. Yan, C. Zhang, J. Yao, Y. S. Zhao, *Adv. Mater.* **25**, 3627–3638 (2013).
3. B. Zhou, G. Xiao, D. Yan, *Adv. Mater.* **33**, e2007571 (2021).
4. W. Yao *et al.*, *Angew. Chem. Int. Ed.* **52**, 8713–8717 (2013).
5. Y. Liu *et al.*, *Angew. Chem. Int. Ed.* **59**, 4456–4463 (2020).
6. Q. H. Cui, Y. S. Zhao, J. Yao, *Adv. Mater.* **26**, 6852–6870 (2014).
7. S. Li, B. Lu, X. Fang, D. Yan, *Angew. Chem. Int. Ed.* **59**, 22623–22630 (2020).
8. X. Ye *et al.*, *Nat. Commun.* **10**, 761 (2019).
9. J. Zhao *et al.*, *J. Am. Chem. Soc.* **141**, 15755–15760 (2019).
10. H. Luo *et al.*, *Adv. Funct. Mater.* **24**, 4250–4258 (2014).
11. M.-D. Qian *et al.*, *Mater. Horiz.* **7**, 1782–1789 (2020).
12. A. Pan *et al.*, *Small* **1**, 980–983 (2005).
13. Z.-F. Chang *et al.*, *Chemistry* **21**, 8504–8510 (2015).
14. Y. Li *et al.*, *ACS Appl. Mater. Interfaces* **9**, 8910–8918 (2017).
15. W. Hu *et al.*, *Adv. Mater.* **26**, 3136–3141 (2014).
16. R. Jin, C. Zeng, M. Zhou, Y. Chen, *Chem. Rev.* **116**, 10346–10413 (2016).
17. I. Chakraborty, T. Pradeep, *Chem. Rev.* **117**, 8208–8271 (2017).
18. Y. Li *et al.*, *Nature* **594**, 380–384 (2021).

19. P. D. Jadzinsky, G. Calero, C. J. Ackerson, D. A. Bushnell, R. D. Kornberg, *Science* **318**, 430–433 (2007).
20. C. Zeng, Y. Chen, K. Kirschbaum, K. J. Lambright, R. Jin, *Science* **354**, 1580–1584 (2016).
21. M. Zhou *et al.*, *Science* **364**, 279–282 (2019).
22. Q. Bao *et al.*, *Adv. Mater.* **22**, 3661–3666 (2010).
23. X. Kang, M. Zhu, *Chem. Soc. Rev.* **48**, 2422–2457 (2019).
24. Q. Li *et al.*, *Science* **378**, 768–773 (2022).
25. N. Goswami *et al.*, *J. Phys. Chem. Lett.* **7**, 962–975 (2016).
26. H. Zhang *et al.*, *Adv. Mater.* **32**, e2001457 (2020).
27. X. Kang *et al.*, *Chem. Sci.* **8**, 2581–2587 (2017).
28. B. Zhou, Z. Qi, D. Yan, *Angew. Chem. Int. Ed.* **61**, e202208735 (2022).
29. M. Zhou *et al.*, *J. Phys. Chem. C* **124**, 7531–7538 (2020).
30. Y. Song *et al.*, *Sci. Adv.* **7**, eabd2091 (2021).
31. Y. Zhen *et al.*, *Inorg. Chem. Front.* **9**, 3907–3914 (2022).
32. X. Yang, X. Lin, Y. Zhao, Y. S. Zhao, D. Yan, *Angew. Chem. Int. Ed.* **56**, 7853–7857 (2017).
33. H. Li *et al.*, *J. Am. Chem. Soc.* **144**, 4845–4852 (2022).
34. M. Shyamal *et al.*, *J. Photochem. Photobiol. Chem.* **342**, 1–14 (2017).

SUPPLEMENTARY MATERIALS

science.org/doi/10.1126/science.adh2365
Materials and Methods
Supplementary Text
Figs. S1 to S32
Tables S1 and S2
References (*35–37*)